INTERNATIONAL JOURNAL OF CLIMATOLOGY
Int. J. Climatol. (2016)
Published online in Wiley Online Library
(wileyonlinelibrary.com) DOI: 10.1002/joc.4702

RMetS
Royal Meteorological Society

ENSO-related moisture and temperature anomalies over South America derived from GPS radio occultation profiles

P. Llamedo,[a]* R. Hierro,[a] A. de la Torre[a] and P. Alexander[b]
[a] *Facultad de Ingeniería, Universidad Austral, Buenos Aires, Argentina*
[b] *Facultad de Ciencias Exactas y Naturales, Universidad de Buenos Aires, Argentina*

ABSTRACT: El Niño Southern Oscillation- (ENSO) related anomaly patterns of monthly specific humidity (q), precipitable water content (PW) and temperature (T) over South America are analysed using the FORMOSAT-3/COSMIC mission data (August 2006–December 2013). The Global Positioning System radio occultation (GPS RO) technique provides high vertical resolution profiles of atmospheric properties (refractivity, density, temperature and water vapour pressure) with a global coverage under any weather condition. During the ENSO warm phase (or El Niño), positive PW anomalies are found over the equatorial Pacific Ocean, southeastern Brazil, Bolivia, Paraguay and northern Argentina. Negative anomalies are found in the northern part of South America, but covering a smaller area. During the ENSO cold phase (or La Niña), positive anomalies are found in the northern part of the continent whereas negative anomalies are found over the Amazon Basin region. A Morlet continuous wavelet transform analysis is applied to deseasonalized PW anomaly time series. Over the areas showing PW anomalies related to ENSO, main modes of oscillation between 35 and 38 months are found, similar to the main oscillation mode of the Oceanic Niño index. Consistent with previous studies, PW anomalies in almost all these areas show a general behaviour towards opposite signals during the opposite ENSO phases. q patterns show a linear (in phase with Oceanic Niño Index) response to ENSO along the equator below 8 km height. The Andes mountains separate positive (west) from negative (east) anomalies during El Niño (EN) events (reversing during LN). The higher q positive anomalies are found over the equatorial Pacific Ocean and over 60°–50°W, 35°–20°S during EN months. T patterns show positive anomalies in the whole tropical troposphere during EN months, with higher values over the equatorial Pacific, west of the Andes between 7 and 15 km height.

KEY WORDS ENSO; FORMOSAT-3/COSMIC; precipitable water; South America

Received 17 December 2014; Revised 1 December 2015; Accepted 21 January 2016

1. Introduction

South America (SA) weather and climate are strongly affected by the topography and the vegetation features as well as by the adjacent oceans (Garreaud *et al.*, 2008). Roughly enclosed between 10°N–55°S and 34°–81°W, SA presents diverse weather patterns including tropical, subtropical and mid-latitudes features. The Andes mountain range, the longest in the world, extends from north to south along the west coast of SA. With an average height of about 4 km (40°S–Equator), it represents a formidable barrier against tropospheric flow, acting as a climate wall (Garreaud *et al.*, 2008). The Amazon basin region (0°–20°S and 75°–45°W), constitutes the largest extent of tropical rainforest on Earth. The annual regional precipitation becomes the main heat source for the tropical atmosphere, providing almost 15% of the global water discharged to the oceans (Richey *et al.*, 2004).

The El Niño Southern Oscillation (ENSO) is the largest signal in the climate system on interannual timescales to cause global climate variability (Rasmusson and Arkin, 1985; Ropelewski and Halpert, 1987). The ENSO alternates in an irregular cycle lasting between 2 and 7 years. The warm ENSO phase or El Niño (EN) episode is characterized by higher than average sea surface temperatures (SST) in the central and eastern equatorial Pacific Ocean, a reduced strength of the easterly trade winds in the Tropical Pacific, and an eastward shift in the region of intense tropical rainfall. Opposite, the cold ENSO phase or La Niña (LN) episode is characterized by unusually cold SST in the same region.

ENSO-induced precipitation and temperature anomalies over several regions (including SA) have been studied by many authors (among others Ropelewski and Halpert, 1987; Ropelewski and Halpert, 1989; Aceituno, 1988; Grimm *et al.*, 2000; Grimm, 2003 and Vera *et al.*, 2004). Ropelewski and Halpert (1987, 1989) identified ENSO-induced precipitation anomalies over northeastern South America (NSA) and southern South America (SSA). NSA, including north equatorial Brazil, French Guiana, Surinam, Guiana and Venezuela, presents dry (wet) precipitation anomalies during the months of March, April and May (MAM) for EN (LN) events. In SSA, the region covering southern Brazil, northeastern Argentina

* Correspondence to: P. Llamedo, Facultad de Ingeniería, Universidad Austral, Mariano Acosta 1611, Pilar B1629ODT, Argentina. E-mail: pllamedo@austral.edu.ar

and Uruguay presents wet (dry) precipitation anomalies during the whole EN (LN) period. Grimm *et al.* (2000) analysed precipitation anomalies associated with EN and LN events over SSA using monthly data from 134 stations during the period 1956–1992. Eight different coherent regions during the EN events and six during the LN events were identified. Six of them are almost the same regions showing a general behaviour towards opposite signals in the precipitation anomalies during the respective EN and LN cycles. The area of largest impact during EN events on precipitation is southern Brazil. More recently, Garreaud *et al.* (2008) used station data and atmospheric reanalysis to show that precipitation anomalies during EN (LN) episodes are negative (positive) in tropical SA (December to March), positive (negative) over the southeastern SA and central Chile, and temperature anomalies are positive (negative) over tropical and subtropical latitudes. With smaller amplitude, a decadal and interdecadal signal can be found in the precipitation records over SA. The main low frequency fluctuation is the Pacific Decadal Oscillation (PDO) (Mantua *et al.*, 1997). Andreoli and Kayano (2005) suggest that the ENSO is modulated by the lower frequency PDO, with stronger anomalies when the EN (LN) take place during the warm (cold) phase of the PDO.

Besides surface stations, several satellite missions observe a variety of parameters related to the atmospheric hydrological response to ENSO, such as precipitation, latent heating and water vapour. In particular, the Global Positioning System (GPS) Radio Occultation (RO) limb sounding technique provides vertical profiles of atmospheric properties such as refractivity, from which density (ρ), pressure (P), temperature (T) and water vapour pressure (e) are derived. It is important to note that additional meteorological information is required to derive e in the middle and lower troposphere. The Constellation Observing System for Meteorology, Ionosphere and Climate (COSMIC) uses the The 1D-Var method technique (Healy and Eyre, 2000) to retrieve both e and T profiles. 1D-Var method is an effective way to combine information provided by GPS RO and a priori atmospheric state in a statistically optimal way. A priori data from the European Centre for Medium-Range Weather Forecasts is used. The vertical resolution of RO profiles ranges from 0.1 km in the lower troposphere to 1.4 km in the stratosphere (Kursinski *et al.*, 1997). The COSMIC mission (Anthes *et al.*, 2008) started in April 2006 and delivers approximately 2000 daily profiles. This technique operates under any weather condition and provides a global coverage. However, the profiles have no regular distribution across the globe and over time. These characteristics and the high vertical resolution of the RO data provide a more detailed view of the 3-dimensional ENSO structure than other observational data sets (Scherllin-Pirscher *et al.*, 2012). Teng *et al.* (2013) found that the global seasonal distributions of COSMIC precipitable water content (PW) associated with the ENSO events exhibit a high correlation with the observed precipitation rate over the ocean from the Special Sensor Microwave Imager (SSM/I) and the Advanced Microwave Scanning Radiometer for EOS (AMSR-E). Recently, Sun *et al.* (2014) showed that the COSMIC-derived indices are significant for ENSO signature monitoring. Furthermore, Hierro *et al.* (2012) studied the capability of the GPS RO to reproduce global, synoptic and regional climatological patterns over South America.

The present work used COSMIC GPS RO data to study the spatial patterns of ENSO-related anomalies over SA. It is organized in four main sections. Section 2 illustrates the data and methodology. The results are presented in Section 3 and finally the conclusions are summarized in Section 4.

2. Data and methodology

COSMIC postprocessed level 2 (Version 2010.2640) 'wet' vertical profiles provide T, P and e from near the surface up to 40 km, interpolated every 0.1 km. Data are binned into longitude, latitude, altitude and time grid cells. Then, the data are averaged using different grid cell sizes, according to the process to be shown (Hierro *et al.*, 2013). From COSMIC e, the specific humidity (q) is calculated as:

$$q = 0.622 \frac{e}{P_d + e} \tag{1}$$

where P_d is the partial pressure of the dry air. The PW [in (millimeter)] is defined as follows:

$$PW = \frac{1}{g} \int_{P_s}^{P_t} q dp \tag{2}$$

where P_S and P_t are the pressure at the surface and at the top of the atmosphere, respectively. More than 90% of COSMIC soundings penetrate the lowest 2 km (and more than 72% the lowest 1 km), however, it is important to note that usually they do not reach the surface. This lack of information between the surface and the lowest point of the RO sounding may lead to an underestimation of PW. To improve the PW estimation, the missing values are filled with the value of q at the lowest point of each sounding (Teng *et al.*, 2013).

The Oceanic Niño Index (ONI) is used for monitoring the ENSO development. This is a 3 month running mean of Extended Reconstructed Sea Surface Temperature (ERSST.v3b) anomalies in the Niño 3.4 region (5 N–5 S, 120–170 W) with respect to the climate average (1971–2000) (Smith *et al.*, 2008). The LN (cold) and EN (warm) episodes are defined when the threshold (±0.5 °C) is met for a minimum of five consecutive overlapping months.

For monthly analysis purposes, the maximum resolution used is a 5° × 5° latitude–longitude grid cell. In the region defined by (30°–120°W; 60°S–25°N), the number of RO events per cell ranges from 5 to 83 with a median of 27.

To remove the variability not associated with ENSO, a standard multivariate regression analysis is used at each grid point. The following linear model (M) is used:

$$F(t) = M \bullet coeff$$

$$\begin{aligned} F(t) = A_0 + A_1 t + A_2 sin(\omega t) + A_3 cos(\omega t) + A_4 sin(2\omega t) \\ + A_5 sin(2\omega t) + A_6 sin(3\omega t) \\ + A_7 cos(3\omega t) + B_1 \mathrm{QBO1}(t) \\ + B_2 \mathrm{QBO2}(t) + B_3 \mathrm{SF}(t) \end{aligned} \quad (3)$$

where $\omega = 2\pi/12$ is the frequency in cycles per months and *F(t)* represents any GPS RO time series (*T(t)*, *PW(t)* or *q(t)*). A_0 and A_1 are the constant and trend coefficients respectively. $A_2 - A_7$ are the seasonal coefficients including the first two annual harmonics. QBO*1(t)* and QBO*2(t)* are standardized time series representing the Quasi-biennial oscillation (QBO) variations at 30 mb and 50 mb, respectively (http://www.cpc.ncep.noaa.gov/data/indices). SF(t) is the standardized time series representing the solar flux (http://www.esrl.noaa.gov/psd/data/correlation/solar.data). At each grid point, the set of model coefficients that best fit the time series *F(t)* is obtained by least squares:

$$\mathrm{coeff} = \left[A_0, ..., A_7, B_1, ..., B_3\right] = \left(M^t \bullet M\right)^{-1} \bullet M^t \bullet F(t) \quad (4)$$

Then, the modelled time series are subtracted from the GPS RO time series removing the seasonal, QBO and solar dependence ($F'(t) = F(t) - M \bullet \mathrm{coeff}$). This method guarantees that the ENSO and other second order fluctuations remain within the anomalies. Once the data is deseasonalized, ENSO-related anomalies are calculated by taking the average along all EN, LN and neutral ONI months. A 2 months lag for the ONI is used.

Despite the relatively short record, RO data capture the ENSO signal, including two EN (15 months) and four LN (33 months) episodes. The statistical significance of the ENSO-related anomalies is assessed by using the Student's *t*-test. A statistical confidence level of 95% is used.

3. Results

3.1. PW anomalies

Figure 1(a) and (b) show the maps of mean PW anomalies during EN and LN months, respectively. During EN months, positive PW anomalies are found over the equatorial Pacific Ocean, southeastern Brazil, Bolivia, Paraguay and northern Argentina (see regions A and C and their surrounding areas in Figure 1). Negative anomalies are found in the northern part of the continent and over the Pacific Ocean (110°–80°W, 8°–18°S). Areas covered by negative anomalies are smaller than those covered by positive anomalies during EN months. During LN months, statistically significant positive anomalies are found in a small part of Region B but less intense than during EN months (green-dotted contours in Figure 1(b)). Negative anomalies are found over the equatorial Pacific Ocean and are less intense over the Amazon Basin (solid contours in Figure 1(b)). A similar pattern is shown in Figure 11 of Teng *et al.* (2013), with the exception of high positive anomalies over Paraguay and northern Argentina during LN months. It is important to note that Teng *et al.* (2013) averaged over individuals EN and LN events.

The linear view of the atmospheric signal associated with ENSO consists of inverse anomalies during the different ENSO phases (Bradley *et al.*, 1987). Figure 1(c) shows the ENSO linear response (i.e. anomalies during EN months minus anomalies during LN months). Andreoli and Kayano (2005), using rainfall reanalysis data, concluded that the linear approach over South America seems to be appropriate. However, the PW response to ENSO exhibits a linear response only over the equatorial Pacific Ocean. Over the continental part of South America anomalies are greater during EN and a weak linear response can be found over southeastern Brazil and the northern part of the continent. Large differences in amplitude imply that there is significant nonlinearity.

EN-related subtropical convection anomalies in South America modify the large scale cell circulation anomaly between the tropics and subtropics (Grimm, 2003). The vertical velocity omega from the National Centers for Environmental Prediction (NCEP) data, is defined as $\omega = \partial P/\partial z$, where P is pressure and z is the height. Thus, $\omega < 0$ means ascent movement. During EN months, strong and consistent positive (negative) PW anomalies occur in areas with negative (positive) ω anomalies (not shown).

Figure 1(d) shows the ENSO regression coefficients derived using the standard multivariate regression but with a different linear model (Equation (3) + B_4ONI(t)). Regression coefficients show similar values to the ones in Figure 1(c) and are similar to those shown in Figure 2(c) of Scherllin-Pirscher *et al.*, 2012). However, lower values are found over southern Brazil, northeastern Argentina, Paraguay and Uruguay.

Three regions were selected (see Figure 1) due to their different response to ENSO: region A (equator–10°N, 100°–110°W), region B (equator–10°N, 50°–60°W) and region C (20°–30°S, 50°–60°W). Region A, over the equatorial Pacific, is selected to show the lag of COSMIC water vapour with ONI. Region B is representative of areas showing positive anomalies during LN and region C during EN. In Figure 2(a), the time evolution of ONI index and monthly PW anomalies in region A, B and C are shown.

The continuous wavelet transform (CWT) is a powerful tool for studying multi-scale and non-stationary processes occurring over finite spatial and temporal domains (Torrence and Compo, 1998). Its capability to deal with non-stationary signals (Daubechies, 1990) is one of its advantages with respect to the Fourier transform, which can lose information within the temporal (or spatial) domain. The signal is compared against shifted and scaled versions of the so-called base or mother wavelet, obtaining the correlation coefficients as function of scale and position. Thus, for each signal portion, the more similar the signals, the higher the values obtained. This process is repeated for all scales and positions of the mother wavelet. This allows to detect the possible existence of oscillations, their periods and positions, as well to locate short life signals and high frequency like sharp changes. The

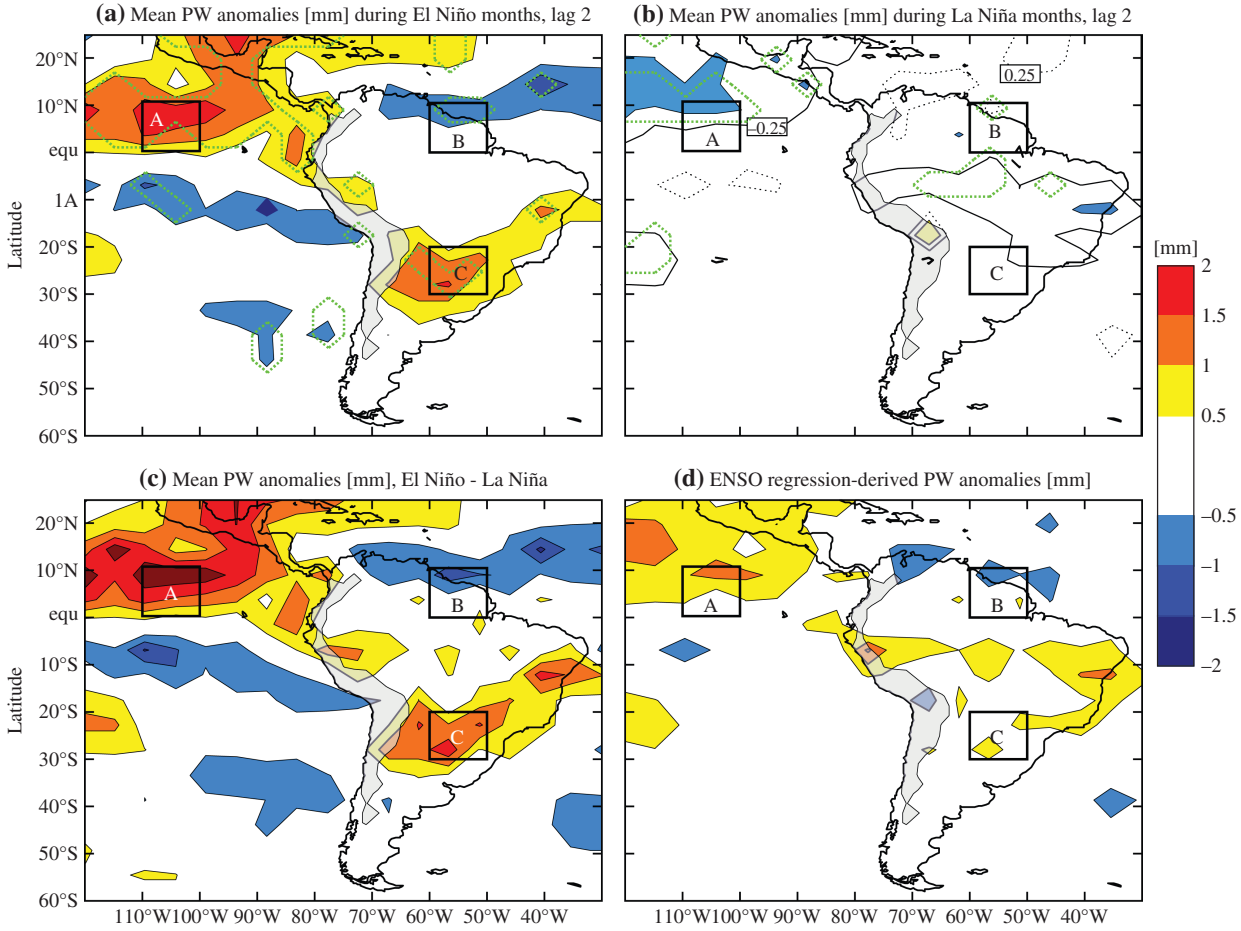

Figure 1. Mean Precipitable Water (PW) related anomalies during (a) El Niño months, (b) La Niña months. (c) Linear response to ENSO, El Niño–La Niña PW anomalies. (d) PW ENSO regression coefficient. The grey mask corresponds to altitudes greater than 2 km. Green-dotted lines encompass values that are, according to the Student's *t*-test, significant at the 95% confidence level.

mother wavelet used was the Morlet wavelet, which consists in a flat wave modified by a Gaussian envelope (Lau and Weng, 1995). This wavelet has been widely used to identify periodic oscillations of real life signals as well as in the analysis of climate-related records (e.g. Lau and Weng, 1995; Yi and Shu, 2012). The use of the Morlet wavelet provides a clear advantage due to its complex nature, which makes it possible to detect time-dependent amplitude and phase for different frequencies (Lau and Weng, 1995). Moreover, the influence of edge effects is well defined for the Morlet wavelet (Torrence and Compo, 1998).

In Figure 2(b), the CWT using a Morlet base is applied to the ONI. Two main modes of oscillation are found, with periods of ≈18 and ≈37 months slightly decreasing towards the end of the timespan. Figures 2(c), (d) and (e) show the Morlet CWT applied to the deseasonalized PW signal corresponding to regions A, B and C, respectively. For regions A, B and C, the longer mode presents a period similar to the ONI index but slightly increasing towards the end of the timespan for region B. For regions A and C, the longer mode disappears beyond 2012 when the ENSO neutral condition starts. Water vapour is well coupled to SST variations over this area, showing the reliability of COSMIC *e*. For region B, two main modes of oscillation are also found. The longer mode has a period of ≈37 months and the shorter mode has a period of ≈20 months. The shorter period is present between January 2008 and January 2012. The original signal can be reconstructed by using an inverse CWT (iCWT). The iCWT applied on the correlation coefficients obtained by the CWT corresponding to certain scales (periods) can be interpreted as a band pass filter for those scales. Figure 2(f) shows the filtered signal corresponding to the periods between 35 and 38 months for the ONI (black), deseasonalized PW in region A (blue), B (red) and C (green). Filtered PW in regions A and C are in phase with ONI index, whereas region B oscillates in counterphase. This reinforces the idea of a linear response to the ENSO in some regions. In this figure, a ≈2–3 months lag is found between ONI and PW anomalies over region A. Other regions which present positive or negative PW anomalies during EN or LN months show a similar behaviour with similar modes of oscillation (not shown).

3.2. Specific humidity anomalies

One of the main advantages of the GPS RO technique is its capability to provide a three-dimensional view of

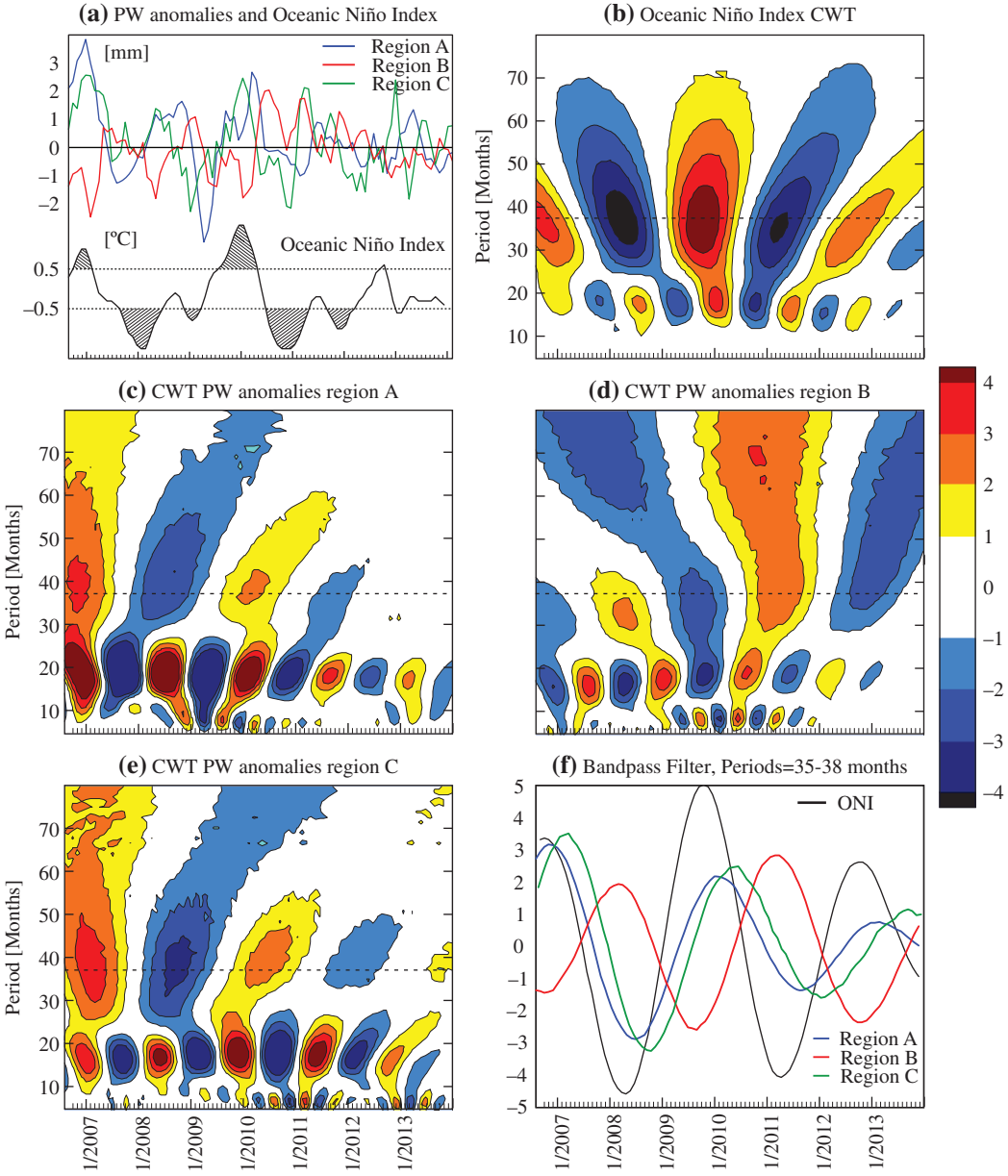

Figure 2. (a) Time evolution of the Oceanic Niño Index (ONI) and monthly PW anomalies in region A, B and C. Morlet Continuous Wavelet Transform for the (b) Oceanic Niño Index, deseasonalized PW in (c) regions A, (d) region B and (e) region C. (f) Filtered signal corresponding to the periods between 35 and 38 months for the ONI (black), deseasonalized PW in regions A (blue), B (red) and C (green).

atmospheric thermodynamic variables with a high vertical resolution. Vertical patterns of the anomalies were analysed by studying different vertical slices. Kishore *et al.* (2011) studied the distribution of water vapour between 50°S and 50°N observed by COSMIC and compared it with radiosonde data sets. A good agreement was found up to 8 km, suggesting that COSMIC water vapour data are reliable in the troposphere.

In particular, three representative slices are analysed: two altitude-latitude slices averaged between 120°–100°W and 50°–60°W, and an altitude-longitude slice averaged between 10°S–10°N. Almost all the ENSO-related anomalies showed in Figure 1(c) are contained in these three slices. Figure 3 shows different vertical slices of deseasonalized q anomalies where the mean is taken during EN (upper row) or LN (lower row) months. Figures 3(a) and (d) show an altitude-latitude slice averaged between 120°–100°W. During EN months, positive anomalies are found between Equator–10°N and 1–8 km height, negative anomalies are found between 20°S–Equator and 2–5 km height. The patterns reverse during LN months and negative anomalies are found between Equator–20°N and 1–8 km height and positive anomalies between 20°S–Equator and 2–5 km height. Figure 3(b) and (e) show an altitude-latitude slice averaged between 60° and 50°W. During EN months, positive anomalies are found between the 35°–15°S and 1–8 km height with the higher anomalies below 5 km. Negative anomalies are found between 45°–40°S and 1–4 km height. During LN months, positive anomalies

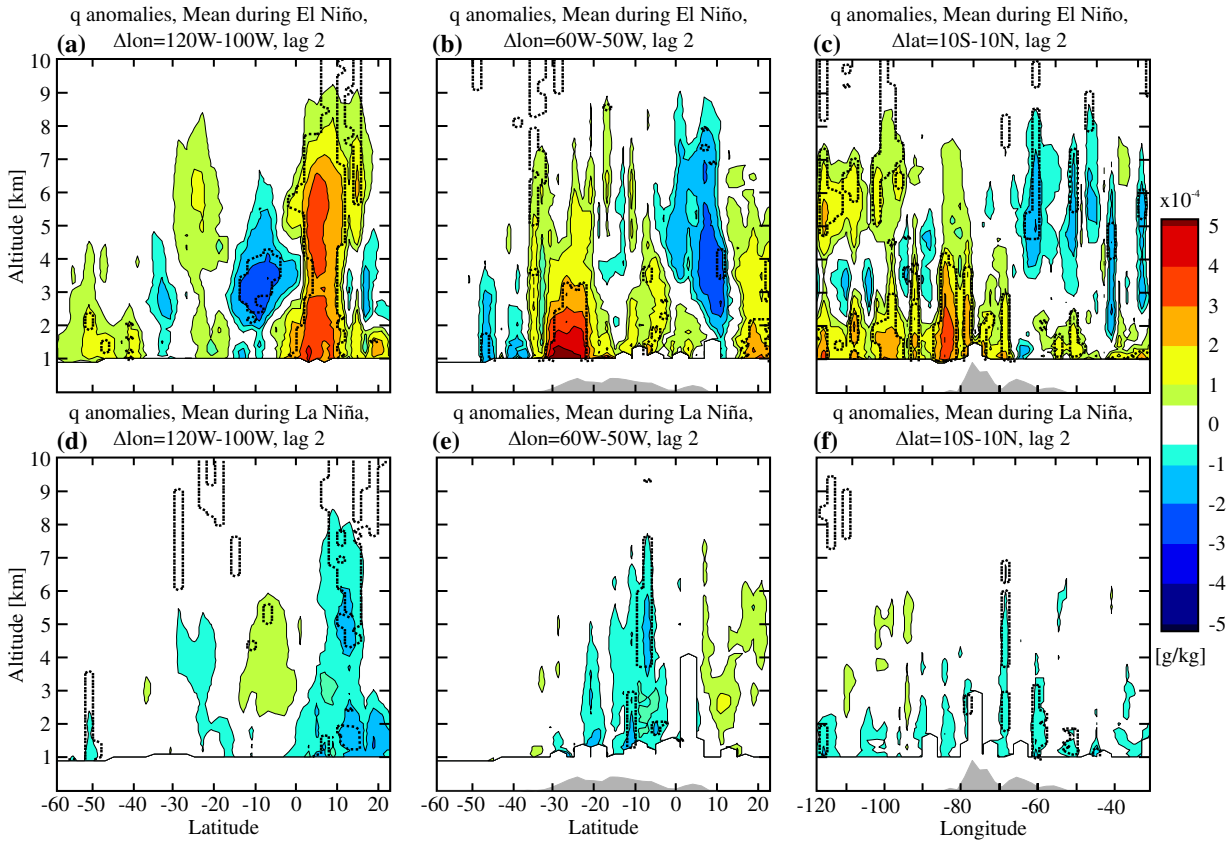

Figure 3. Mean specific humidity related anomalies during El Niño (upper row) and La Niña (lower row) months, (a)–(d) altitude-latitude averaged between 120° and 100°W, (b)–(e) altitude-latitude averaged between 60° and 50 W, (c)–(f) altitude-longitude averaged between 10°S and 10°N. The grey-shaded contour represents the topography. Black-dotted lines encompass values that are, according to the Student's *t*-test, significant at the 95% confidence level.

are found north of the Equator between 2 and 6 km height. Figure 3(c) and (f) show an altitude-longitude slice averaged between 10°S and 10°N. The influence of the Andes range is clearly seen with opposite behaviour east and west of the Andes (see Garreaud *et al.*, 2008). During EN months, positive anomalies are found over the Equatorial Pacific, west of the Andes, between 1 and 8 km height, whereas negative anomalies are found east of the Andes between 2 and 8 km height. During LN months only weak negative anomalies appear.

3.3. Temperature anomalies

Figure 4 shows the same three representative vertical slices as above, but now for the deseasonalized T anomalies, where the mean is taken during EN (upper row) or LN (lower row) months. The possible influence of QBO in the lower tropical stratosphere cannot be ruled out. Although the effects of QBO have been removed via linear regression, the occurrence of residuals coincident with the timing of QBO and ENSO suggest interactions not modelled by the linear QBO and ENSO (Randel and Wu, 2015). QBO influence is important in the negative anomalies along the lower tropical stratosphere (above 20 km height) during EN months (Figure 4(a), (b) and (c)) and positive anomalies during LN months (Figure 4(d), (e) and (f)). However, the negative anomalies found during EN months in the subtropical stratosphere could be associated with ENSO (Figure 4(a) and (b)).

During EN months, T positive anomalies are found in the troposphere between 20°S and 20°N with higher values between 10 and 15 km height (Figure 4(a) and (b)). Similar results were found by Scherllin-Pirscher *et al.*, (2012) and Randel and Wu, (2015). The pattern reverses during LN months, but with weaker anomalies. Figure 4(b) and (e) show an altitude-latitude slice averaged between 60 and 50 W. Positive anomalies are found from 35°S to 25°N from 3 km height to the tropopause, with the higher values in 35°–20°S. During EN months, positive anomalies are found in the whole tropical troposphere (Figure 4(c)), with higher values over the equatorial Pacific, west of the Andes between 7 and 15 km height. East of the Andes, weak positive anomalies are found above ∼7 km up to the tropopause. The warming of the troposphere is a well-known feature of ENSO (Calvo Fernández *et al.*, 2004; Scherllin-Pirscher *et al.*, 2012).

At higher latitudes (60°–45°S), positive (negative) anomalies are found in the southern Pacific Ocean (Figure4 (a)) below (above) the tropopause during EN months. In the southern part of the continent (Figures4 (b) and (e)), negative anomalies are found in the stratosphere (above 15 km height) during EN months, reversing with less intensity during LN.

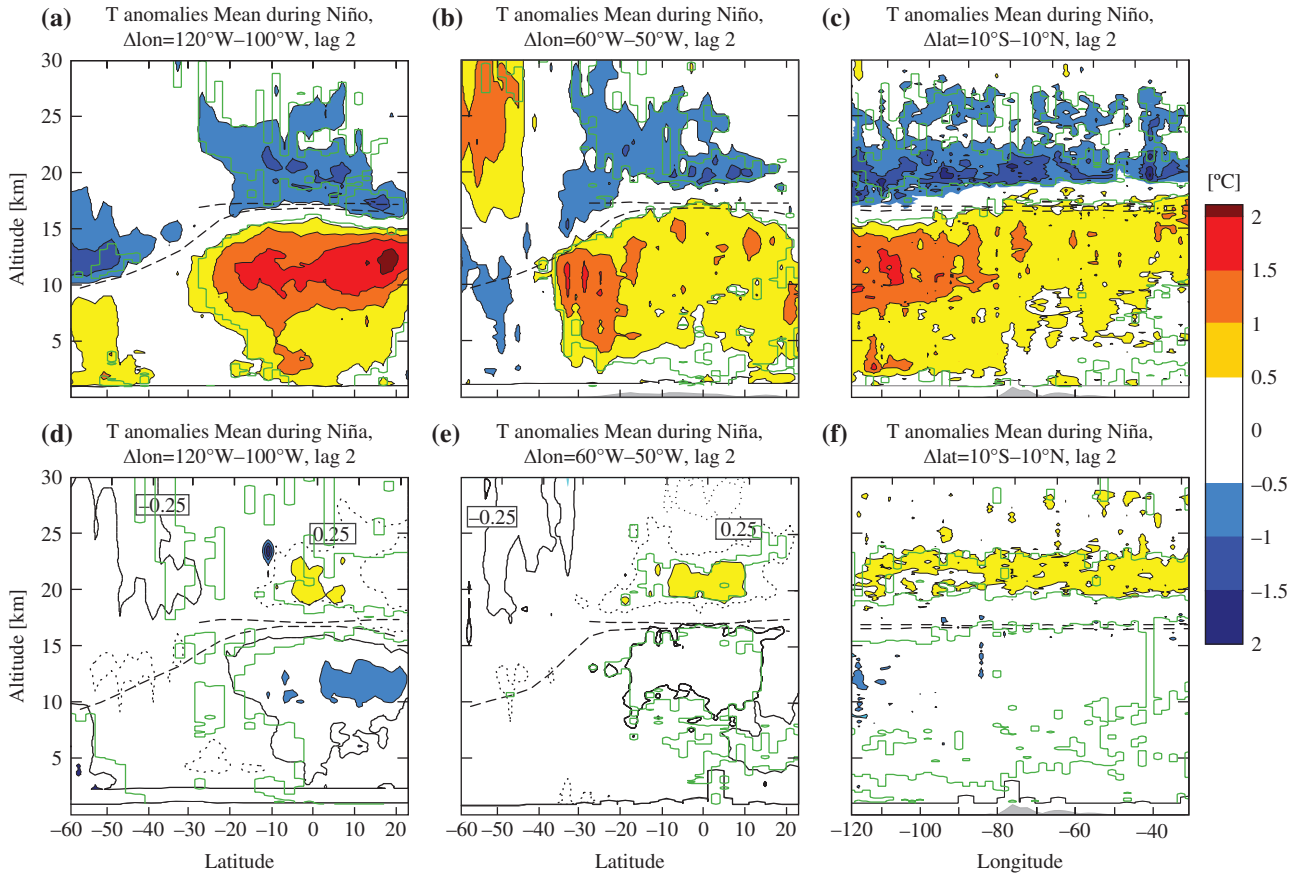

Figure 4. Mean temperature-related anomalies during El Niño (upper row) and La Niña (lower row) months, (a)–(d) altitude-latitude averaged between 120° and 100°W, (b)–(e) altitude-latitude averaged between 60° and 50°W, (c)–(f) altitude-longitude averaged between −10°S and 10°N. The grey-shaded contour represents the topography. Dotted lines denote the mean lapse-rate tropopause (LRT) and the cold point tropopause (CPT) altitude. Green contours encompass values that are, according to the Student's *t*-test, significant at the 95% confidence level.

4. Summary

COSMIC GPS RO data were used to investigate the ENSO-related anomaly patterns of monthly PW, q and T over South America. Despite the relatively short data record, RO data clearly capture the ENSO signal, as can be seen in the wavelets analysis of deseasonalized anomalies. Over the areas showing PW anomalies related with ENSO, two main modes of oscillation between 35 and 38 months and 18 and 20 months are found, similar to the main oscillation modes for the ONI. These modes oscillate in phase or counterphase with respect to the ONI. With the actual amount of RO data, the highest possible resolution for monthly analysis is about 5° × x5° latitude–longitude grid cell, with a median of 27 RO events per grid cell/month. During the ENSO warm phase (or El Niño) PW positive anomalies are found over the equatorial Pacific Ocean, southeastern Brazil, Bolivia, Paraguay and northern Argentina. Negative anomalies are found in the northern part of the continent, but covering a smaller area. During the ENSO cold phase (or La Niña), positive anomalies are found in the northern part of the continent whereas weak negative anomalies are found over the Amazon Basin region. q patterns show a linear [in phase with Oceanic Niño Index (ONI)] response to ENSO along the Equator below 8 km height. The Andes mountains separate positive (west) from negative (east) anomalies during EN events (reversing during LN). The higher positive anomalies are found over the equatorial Pacific Ocean and over 60°–50°W, 35°–20°S during EN months. Consistent with previous studies, almost all these areas show a general behaviour towards opposite signals during the opposite ENSO phases, but with a weaker signal during LN. Furthermore, T anomalies show the well-known warming of the troposphere during EN months. The possible influence of QBO in the lower tropical stratosphere cannot be ruled out. Due to the possible nonlinear interaction between QBO and ENSO, some QBO residuals may remain in the tropical stratospheric T-related anomalies.

Acknowledgements

Manuscript prepared under Grant CONICET PIP11220120100034, ANPCYT PICT2013-1097. P. Llamedo, R. Hierro, A. de la Torre and P. Alexander are members of CONICET. GPS RO data downloaded from cdaac-ftp.cosmic.ucar.edu. ONI and QBO indices downloaded from http://www.cpc.ncep.noaa.gov/data/indices.

References

Aceituno P. 1988. On the functioning of the Southern Oscillation in the South American sector. Part I: surface climate. *Mon. Weather Rev.* **116**: 505–524.

Andreoli R, Kayano M. 2005. ENSO-related rainfall anomalies in South America and associated circulation features during warm and cold Pacific Decadal Oscillation regimes. *Int. J. Climatol.* **25**: 2017–2030.

Anthes RA, Ector D, Hunt DC, Kuo Y-H, Rocken C, Schreiner C, Sokolovskiy SV, Syndergaard S, Wee T-K, Zeng Z, Bernhardt PA, Dymond KF, Chen Y, Liu H, Manning K, Randel WJ, Trenberth KE, Cucurull L, Healy SB, Ho S-P, McCormick C, Meehan TK, Thompson DC, Yen NL. 2008. The COSMIC/FORMOSAT-3 Mission: Early Results. *Bull. Amer. Meteor. Soc.* **89**: 313–333, doi: 10.1175/BAMS-89-3-313..

Bradley RS, Diaz HF, Kiladis GN, Eischeid JK. 1987. ENSO signal in continental temperature and precipitation records. *Nature* **327**: 497–501.

Calvo Fernández N, Ricardo Garía H, David Gallego P, Emiliano Hernández M, Rolando RG, Luis Gimeno P, Pedro Ribera R. 2004. Analysis of the ENSO signal in tropospheric and stratospheric temperatures observed by MSU, 1979–2000. *J. Clim.* **17**: 3934–3946.

Daubechies I. 1990. The wavelet transform time-frequency localization and signal analysis. *IEEE Trans. Inf. Theory* **36**: 961–1004.

Garreaud RD, Vuille M, Compagnucci R, Marengo J. 2008. Present-day South American climate. *Paleogeogr. Palaeoclimatol. Palaeoecol.*, doi: 10.1016/j.palaeo.2007.10.032.

Grimm AM. 2003. The El Niño impact on the summer monsoon in Brazil: regional processes versus remote influences. *J. Clim.* **16**: 263–280.

Grimm AM, Barros VR, Doyle ME. 2000. Climate variability in Southern South America associated with El Niño and La Niña events. *J. Clim.* **13**: 35–58.

Healy SB, Eyre JR. 2000. Retrieving temperature, water vapour and surface pressure information from refractive-index profiles derived by radio occultation data: a simulation study. *Q. J. R. Meteorol. Soc.* **126**: 1661–1683.

Hierro R, Llamedo P, de la Torre A, Alexander P, Rolla A. 2012. Climatological patterns over South America derived from COSMIC radio occultation data. *J. Geophys. Res.* **117**: D03116.

Hierro R, Llamedo P, de la Torre A, Alexander P. 2013. Oscillation modes of humidity over the Amazon basin derived from GPS RO profiles. *J. Geophys. Res.* **118**: 13,121–13,127.

Kishore P, Venkat Ratnam M, Namboothiri SP, Velicogna I, Basha G, Jiang JH, Igarashi K, Rao SVB, Sivakumar V. 2011. Global (50S-50 N) distribution of water vapor observed by COSMIC GPS RO: Comparison with GPS radiosonde, NCEP, ERA-Interim, and JRA-25 reanalysis data sets. *J. Atmos. Sol.-Terr. Phys.* **73**(13): 1849–1860.

Kursinski ER, Hajj GA, Schofield JT, Linfield RP, Hardy KR. 1997. Observing Earth's atmosphere with radio occultation measurements using the Global Positioning System. *J. Geophys. Res.* **102**: 23429–23465, doi: 10.1029/97JD01569.

Lau K-M, Weng H-Y. 1995. Climate signal detection using wavelet transform: how to make a time series sing. *Bull. Am. Meteorol. Soc.* **76**: 2391–2402.

Mantua NJ, Hare S, Zhang Y, Wallace JM, Francis RC. 1997. A Pacific interdecadal climate oscillation with impacts on salmon production. *Bull. Am. Meteorol. Soc.* **78**: 1069–1079.

Randel WJ, Wu F. 2015. Variability of zonal mean tropical temperatures derived from a decade of GPS radio occultation data. *J. Atmos. Sci.* **72**: 1261–1275.

Rasmusson EM, Arkin PA. 1985. In *Interannual Climate Variability Associated with the El Niño/Southern Oscillation, Coupled Ocean-Atmosphere Models*, Nihoul JCJ (ed). Elsevier Science Publishers. B.V: The Netherlands, 289–302.

Richey J, Victoria E, Mayorga E, Martinelli L, Meade R. 2004. Integrated analysis of a humid tropical region – The Amazon Basin. In *Vegetation, Water, Humans, and the Climate*, Kabat P (ed). Springer-Verlag: Berlin, 415–418.

Ropelewski CH, Halpert S. 1987. Global and regional scale precipitation patterns associated with the El Niño/Southern Oscillation. *Mon. Weather Rev.* **115**: 1606–1626.

Ropelewski CH, Halpert S. 1989. Precipitation patterns associated with the high index phase of the Southern Oscillation. *J. Clim.* **2**: 268–284.

Scherllin-Pirscher B, Deser C, Ho S-P, Chou C, Randel W, Kuo Y-H. 2012. The vertical and spatial structure of ENSO in the upper troposphere and lower stratosphere from GPS radio occultation measurements. *Geophys. Res. Lett.* **39**: L20801.

Smith TM, Reynolds RW, Peterson TC, Lawrimore J. 2008. Improvements to NOAA's historical merged land-ocean surface temperature analysis (1880–2006). *J. Clim.* **21**: 2283–2296.

Sun YY, Liu JY, Tsai HF, Lin CH, Kuo YH. 2014. The Equatorial El Niño-Southern Oscillation signatures observed by FORMOSAT-3/COSMIC from July 2006 to January 2012. *Terr. Atmos. Ocean. Sci.* **25**: 545–558.

Teng W-H, Huang C-Y, Ho S-P, Kuo Y-H, Zhou X-J. 2013. Characteristics of global precipitable water in ENSO events revealed by COSMIC measurements. *J. Geophys. Res.* **118**: 8411–8425.

Torrence C, Compo GP. 1998. A practical guide to wavelet analysis. *Bull. Am. Meteorol. Soc.* **79**: 6178.

Vera C, Silvestri G, Barros V, Carril A. 2004. Differences in El Niño response over the Southern Hemisphere. *J. Clim.* **17**: 1741–1753.

Yi H, Shu H. 2012. The improvement of the Morlet wavelet for multi-period analysis of climate data. *Comptes Rendus Geoscience* **344**: 483–497.

